phys. stat. sol. (a) **203**, No. 8, 1901 – 1914 (2006) / **DOI** 10.1002/pssa.200622014

Editor's Choice

Numerical simulation of impedance and admittance of OLEDs

N. D. Nguyen* and **M. Schmeits**

Institute of Physics, University of Liege, 4000 Sart-Tilman/Liege, Belgium

Received 11 January 2006, revised 22 March 2006, accepted 23 March 2006
Published online 15 May 2006

PACS 72.80.Le, 73.61.Ph, 85.60.Bt, 85.60.Jb

The electrical characteristics of organic light-emitting devices are calculated for the dc and ac regimes by numerically solving the basic semiconductor equations under steady-state and small-signal conditions. For a given structure, the dc and ac electric potential and electric field, the electron and hole concentrations, as well as the different components of the current density are obtained as function of the one-dimensional spatial coordinate. This approach allows a detailed microscopic description of the dependencies of these quantities on the applied steady-state voltage V_0 and the frequency of the modulating voltage. The final output consists in the frequency-dependent complex admittance and impedance of the device, the real and imaginary parts of which are the experimentally-available data. As a typical example, we show the results for a two-layer structure where α-NPD is the hole-transporting material and Alq_3 the electron-transporting material. The anode is made of ITO and Al/LiF composes the cathode. The admittance and impedance curves, yielded by the numerical simulation as functions of the modulation frequency, are fitted by an equivalent electrical circuit, the elements of which are resistances and capacitances. The number of components depends on the structure composition and on the applied steady-state voltage. We show that each element can be associated with a particular region of the device. This allows to correlate the dependence of each feature of the admittance and impedance curves with one or several parameters describing the material system. Such an analysis can be useful for the inverse approach, where, starting from measurements of the electrical ac characteristics, the aim is to get information on the microscopic mechanisms which contribute to the electrical conduction of the device.

© 2006 WILEY-VCH Verlag GmbH & Co. KGaA, Weinheim

1 Introduction

The electrical characteristics of organic diodes made of polymers or small molecules have been widely studied during the last ten years. Applications of these structures are light-emitting diodes (OLED) used in displays or large area illuminating systems, as well as transistors or photovoltaic devices. The study of the electrical characteristics of inorganic and organic diodes contributes, on the one hand, to the understanding of the basic physics of the transport mechanisms, and, on the other hand, to the optimizing of the performances of the devices. For the latter, ready-to-use representations of the material systems in terms of equivalent electrical circuits can be conveniently used. Examples of experimental admittance or impedance studies are given in Refs. [1 – 15].

In this paper, we present a theoretical study of the electrical conduction in organic devices under small-signal conditions. The devices of interest are built with one or several layers of organic materials. Carriers are injected through metallic electrodes and, after transport through layers of high carrier mobility, they radiatively recombine, producing visible light [1]. The polymeric or low-molecular weight ma-

* Corresponding author: e-mail: nd.nguyen@ulg.ac.be, Phone: +32 4 366 3722, Fax: +32 4 366 2990

WILEY InterScience® DISCOVER SOMETHING GREAT

© 2006 WILEY-VCH Verlag GmbH & Co. KGaA, Weinheim

terials are treated within a description derived for inorganic semiconductor devices and usually called the drift-diffusion formalism. This framework allows the use of conduction and valence bands, assuming that free carrier transport is characterized by electron and hole mobilities. Application to structures made of organic materials may be considered as a first approximation, due to the inherent complexity of these materials. The assumption of band transport with determined mobilities for electrons and holes, which is not fully compatible with the amorphous nature of the organic layers, might thus lead to difficulties in the interpretation of the results, due to discrepancies in charge transport between organic and inorganic materials. However, in spite of its limitations, this approach allows a tractable description of the electrical conduction process. It is widely spread in literature and has been successfully applied to OLEDs (see [16] and references therein). The analysis starts with the classical semiconductor equations which are generally used in the description of electronic devices [17]. This equation set includes Poisson's equation for the electric potential and continuity equations for electrons and holes.

The numerical simulation is performed for a typical structure in order to illustrate the microscopic response of the organic medium to the applied ac voltage. The device that we have chosen to simulate contains α-NPD as hole transport material and Alq_3 as electron transport material; the latter is also the host of the recombination process. No particular dye molecules are included as recombination centres. Indium tin oxide (ITO) acts as the hole injection contact and Al/LiF is taken as composition of the electrode close to the Alq_3 layer. A set of parameters is used to characterize the materials of the different layers, the contacts and the experimental conditions, such as temperature, applied voltage and modulation frequency. In the first step of the calculations, the equations are solved for the steady-state condition. This yields the energy band diagram, the electron and hole distributions, as well as the current densities and the recombination rates. The position-dependent amplitudes of the same quantities are then obtained by the small-signal analysis. These results lead, for a given steady-state voltage, to the admittance- and impedance-versus-frequency curves which are the macroscopic quantities that can be compared to experiment. Then, a relation between the microscopic effects of the applied modulating voltage and the characteristics of the admittance spectra can be established. The philosophy that guided the present work is similar to that used for numerical studies of steady-state conduction of organic diodes which can be found in the Refs. [18–24].

In the final step, the admittance and impedance curves obtained from numerical simulation are fitted by equivalent electrical circuit models, as it is classically done in the analysis of experimentally-obtained results. The number of elements (resistances and capacitances) and their association depend on the composition of the structure, essentially the number of layers, their dopant concentrations and the contacts. The equivalent circuit is also function of the applied steady-state voltage and the temperature. In our study, we show that each component of the circuit can be associated with a particular region of the device, for example a depletion layer close to a contact or part of a bulk transport layer. As a consequence, it is possible to study the effect of each parameter used in the simulation on the values of one or several elements of the equivalent circuit. The advantage of this investigation is to establish the electrical model for a structure which is well-defined. The disadvantage is that the description supposes that contacts are ideal, layers are homogeneous and interfaces consist in perfect discontinuities, in contrast to real devices where leakage currents may occur and interfaces contain non-homogeneous regions which are comparable in size to that of the molecules composing the different layers. The electrical characteristics of the ideal structure could therefore present features which are smeared out in a real device.

The paper is organized as follows. In Section 2, the basic formal developments of the numerical calculations are given. Results of the application to a typical device are shown in Section 3. We summarize the discussion and conclude the paper in Section 4.

2 Basic formalism

We start from the basic equations for semiconductor devices [17], and extend these to materials of organic compounds. The formal developments are applied to a structure with planar geometry comprising one or several organic layers sandwiched between two metallic electrodes. Therefore, all quantities de-

© 2006 WILEY-VCH Verlag GmbH & Co. KGaA, Weinheim

pend only on one spatial variable x. The treatments generally used to study devices made of inorganic substances are applied to the organic materials. The occupied HOMO levels play the role of the valence band and the unoccupied LUMO levels give the conduction band. They are separated by an empty gap of value E_g. Assuming Boltzmann statistics, the free electron and hole concentrations are given in terms of the electron and hole quasi-Fermi levels F_n and F_p by

$$n = N_c \exp\left[(F_n - E_c)/kT\right] , \tag{1}$$

$$p = N_v \exp\left[\left(E_v - F_p\right)/kT\right] , \tag{2}$$

where E_c and E_v are respectively the conduction and valence band edges and N_c and N_v the effective conduction and valence band densities of states. The band edges E_c and E_v are position-dependent and related to the electrostatic potential ψ by

$$E_c = -\chi - q\psi , \tag{3}$$

$$E_v = -\chi - q\psi - E_g , \tag{4}$$

where χ is the electron affinity. It defines the position of the various energy levels with respect to a common zero reference level. Defects states either of donor or acceptor type can eventually be included [25], but will not be considered farther in this work. The electrical potential ψ obeys Poisson's equation

$$\varepsilon \frac{\mathrm{d}^2}{\mathrm{d}x^2} \psi = -q(p - n + N_D - N_A) , \tag{5}$$

where N_D and N_A are the shallow donor and acceptor concentrations. The continuity equations for electrons, holes are

$$\frac{\partial n}{\partial t} = \frac{1}{q} \frac{\mathrm{d}}{\mathrm{d}x} J_n - R_{bb} , \tag{6}$$

$$\frac{\partial p}{\partial t} = -\frac{1}{q} \frac{\mathrm{d}}{\mathrm{d}x} J_p - R_{bb} . \tag{7}$$

In these equations, J_n and J_p are the electron and hole current densities consisting of a drift and a diffusion contribution. As degeneracy effects are neglected, classical Einstein relations between diffusion constants (D_n for electrons and D_p for holes) and carrier mobilities are assumed. R_{bb} is a band to band recombination term, which is given by a Langevin expression [21]

$$R_{bb} = \frac{q}{\varepsilon_r \varepsilon_0} (\mu_e + \mu_h)(np - n_i^2) , \tag{8}$$

where ε_r is the relative dielectric constant of the material, n_i is the intrinsic carrier density and μ_e and μ_h are the electron and hole carrier mobilities. Recombination terms implying deep traps in the forbidden gap could be included. The mobilities are supposed to be field-dependent, following a Poole–Frenkel law [21]

$$\mu(E) = \mu_0 \exp\left(\sqrt{\frac{E}{E_0}}\right) . \tag{9}$$

Here μ_0 is the zero-field mobility and E_0 is the characteristic electric field. Dependence of carrier mobility on charge density is neglected.

In the study of the ac response under small-signal conditions, a sinusoïdal voltage of amplitude $\tilde{V} \ll kT/q$ and of frequency $f = \omega/2\pi$ is added to the steady-state voltage V_0:

$$V = V_0 + \tilde{V}\, \mathrm{e}^{j\omega t} . \tag{10}$$

 © 2006 WILEY-VCH Verlag GmbH & Co. KGaA, Weinheim

physica status solidi a

Within the small-signal approximation, all quantities can be written as the sum of a steady-state plus a harmonic term. All higher order terms are neglected. Labelling the steady-state term with an index 0 and the ac component with a tilde, one has e.g. for the potential, the electron concentration and the hole concentration

$$\psi(x,t) = \psi_0(x) + \tilde{\psi}(x)\,\mathrm{e}^{j\omega t}\,, \tag{11}$$

$$n(x,t) = n_0(x) + \tilde{n}(x)\,\mathrm{e}^{j\omega t}\,, \tag{12}$$

$$p(x,t) = p_0(x) + \tilde{p}(x)\,\mathrm{e}^{j\omega t}\,. \tag{13}$$

The amplitude of the various ac terms is complex in the general case, as these quantities are not in phase with the applied voltage.

As for the steady-state case, the ac problem can be reduced to a set of three equations, obtained by introducing the harmonic developments (11)–(13) in the expression of Poisson's equation and the continuity equation for electrons and holes. The as-obtained equations are written in terms of the variables $\tilde{\psi}$, $\tilde{n}$ and $\tilde{p}$. In addition to the electron and hole ac current densities $\tilde{J}_{\mathrm{n}}$ and $\tilde{J}_{\mathrm{p}}$, the total current density contains the displacement current term $\tilde{J}_{\mathrm{D}} = \varepsilon\,\partial E/\partial t$. The sum of these three terms yields the total current which has to be constant with respect to position x.

For the numerical resolution of both the steady-state and small-signal equations, one expresses all terms as functions of the electrical potential ψ and of the electron and hole Fermi-levels F_{n} and F_{p}, using relations (1) and (2) for the steady-state part. For the ac components of n and p, one obtains by inserting relations (12) and (13) into (1) and (2), making use of (3) and (4), and retaining only first order terms

$$\tilde{n} = n_0(q\tilde{\psi} + \tilde{F}_{\mathrm{n}})/kT\,, \tag{14}$$

$$\tilde{p} = -p_0(q\tilde{\psi} + \tilde{F}_{\mathrm{p}})/kT\,. \tag{15}$$

The steady-state and small-signal equations are of similar form, they therefore can be solved along the same numerical procedure. After scaling and discretisation according to a variable size mesh, the resulting second-order non-linear equations are linearized in terms of small corrections of the variables and iterated until convergence is achieved.

Contacts are supposed to be of the Schottky type, where electron and hole currents at the contacts are specified at the left contact x_{L} and the right contact x_{R}. In the expression of the boundary conditions, each contact current consists of a thermionic and recombination current J_1 plus a tunnelling term J_2 [16]. The first term J_1 can be expressed in terms of a surface recombination velocity and writes respectively for electrons and holes:

$$J_{1\mathrm{n}} = qv_{\mathrm{sn}}(n - n_{\mathrm{eq}})\,, \tag{16}$$

$$J_{1\mathrm{p}} = qv_{\mathrm{sp}}(p - p_{\mathrm{eq}})\,, \tag{17}$$

where n_{eq} and p_{eq} are respectively the electron and hole thermal equilibrium values at the contacts.

The surface recombination velocities are given in terms of the carrier mobilites [26], which yields for the electronic term

$$v_{\mathrm{sn}} = \frac{16\pi\varepsilon_{\mathrm{s}}\varepsilon_0(kT)^2\mu_{\mathrm{n}}}{q^3}\,, \tag{18}$$

with a similar expression for the hole recombination velocity v_{sp}. The electron and hole current densities J_2 at the contacts are the Fowler–Nordheim tunneling currents. The electron term is written

$$J_{2\mathrm{n}} = \alpha_{\mathrm{t}}\left(\frac{B}{\phi_{\mathrm{bn}}}\right)E^2 \exp\left\{-\alpha_{\mathrm{b}}C\left[\frac{(q\phi_{\mathrm{bn}})^{3/2}}{E}\right]\right\}, \tag{19}$$

© 2006 WILEY-VCH Verlag GmbH & Co. KGaA, Weinheim

where ϕ_{bn} is the barrier height and $B = q^3/(8\pi h)$ and $C = 8\pi\sqrt{2m}/(3hq)$. α_t and α_b are adjustable parameters allowing for eventual corrections to take into account for the inadequate field dependence of these expressions. Image force lowering is also included.

This yields all dc and ac components of the involved physical quantities. The small-signal conductance G and capacitance C are obtained from the complex admittance $Y = \tilde{J}/\tilde{V}$ which is decomposed into an equivalent parallel conductance and capacitance

$$Y = G(\omega, V_0) + j\omega C(\omega, V_0) \, . \tag{20}$$

The impedance is defined as the inverse of the admittance $Z = 1/Y$ and is decomposed into its real and imaginary part

$$Z = \mathrm{Re}\, Z(\omega, V_0) + j\, \mathrm{Im}\, Z(\omega, V_0) \, . \tag{21}$$

These quantities can be compared with experimentally obtained admittance or impedance data.

3 Numerical results

3.1 General characteristics of the simulated device

The formal developments described in Section 2 are applied to a material system whose composition is characteristic of most OLED structures. It consists of a two-layer system, containing α-NPD and Alq_3 as active components. These are, respectively, typical hole transport and electron transport materials. The total thickness of the layers is of 100 nm and the section A has been taken equal to 0.2 cm^2. The anode is ITO and LiF/Al compound forms the cathode. The very thin LiF layer allows to increase the device efficiency by modifying the Al work function and introducing n-doping to the electron transport material [27, 28]. This system operates as an OLED with Alq_3 acting as emitting material, as radiative recombination takes place on the Alq_3-side of the heterointerface. The set of parameters chosen for the numerical study are given in Table 1. The hole transport layer, α-NPD, is weakly doped with a background doping level of $N_A = 1 \times 10^{16}$ cm^{-3}, the Alq_3 layer is supposed to be n-doped with Li atoms originating by diffusion from the LiF sheet close to the Al contact. This doping is space-dependent and is taken as $N_D(x) = N_{DR} \times \exp{(x - x_R)/x_d}$, with $N_{DR} = 1 \times 10^{18}$ cm^{-3} and $x_d = 40$ nm. The ITO/α-NPD interface shows a nearly ohmic contact behavior with a barrier height of 0.3 eV for holes. The barrier height of 0.65 eV for the Alq_3/LiF/Al interface is such that tunneling effects determine the electrical characteristics. The coefficients α_t and α_b in the expression of the tunnelling current given by relation (19) have been taken equal to 1.

Table 1 Set of parameters used for numerical simulation.

parameter	α-NPD	Alq_3
layer thickness (nm)	50	50
dielectric constant ε_r	3	3
E_{HOMO}/vacuum (eV)	–5.5	–5.7
E_g (eV)	3.1	2.7
valence band DOS N_v (cm^{-3})	1×10^{21}	1×10^{21}
conduction band DOS N_c (cm^{-3})	1×10^{21}	1×10^{21}
acceptor concentration N_A (cm^{-3})	1×10^{16}	
donor concentration N_D (cm^{-3})		$N_{D0}\exp[(x-x_R)/x_d]$ $N_{D0} = 1 \times 10^{18}$ cm^{-3}, $x_d = 40$ nm
electron zero-field mobility μ_{e0} (cm^2/V s)	8×10^{-5}	1×10^{-7}
electron characteristic field E_{e0} (V/cm)	2.17×10^5	3.56×10^4
hole zero-field mobility μ_{h0} (cm^2/V s)	8×10^{-4}	1×10^{-8}
hole characteristic field E_{h0} (V/cm)	2.17×10^5	3.56×10^4

 © 2006 WILEY-VCH Verlag GmbH & Co. KGaA, Weinheim

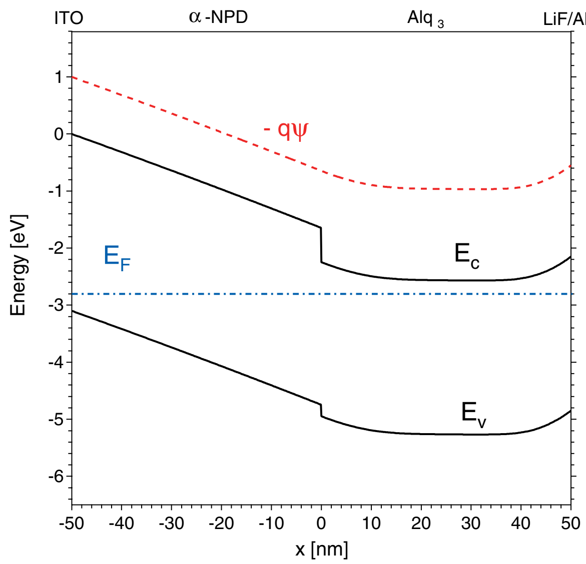

Fig. 1 Energy band diagram at thermal equilibrium for ITO/α-NPD/Alq_3/LiF-Al structure with parameter set given in Table 1. Conduction band edge at left contact is taken as zero of energies.

3.2 Steady-state solution

The energy band diagram at thermal equilibrium (zero applied voltage) is shown in Fig. 1. The Fermi level E_F, which is constant along x, coincides with the electron and hole quasi-Fermi levels F_n and F_p and joins the values of the Fermi energies of the metal at the contacts. Due to the small charge concentration in the α-NPD layer, the electrical potential and, consequently, the conduction and valence band edges, vary linearly for $x < 0$ nm.The band diagram for $x > 0$ is determined by the exponential donor doping concentration in the Alq_3 layer. The configuration is nearly bulk-like in the region from 10 nm to 40 nm.

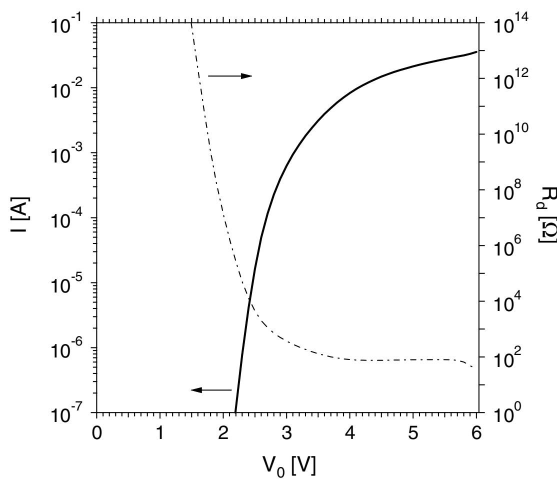

Fig. 2 Current I as function of applied voltage V_0 for structure of section $A = 0.2$ cm^2, and differential resistance $R_d = (dI/dV)^{-1}$ as function of applied voltage.

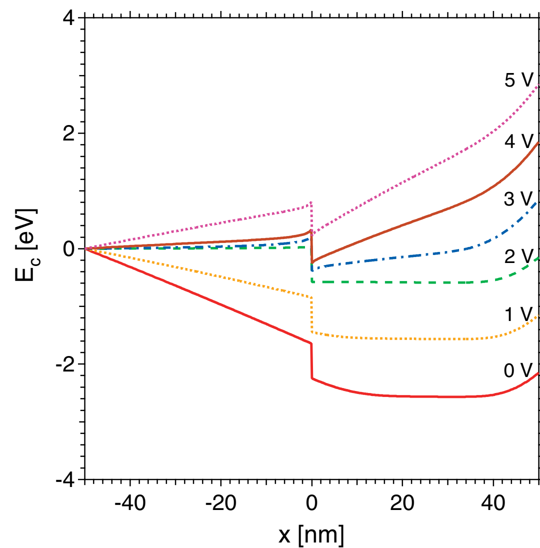

Fig. 3 Conduction energy band edge E_c as function of position x for applied steady-state voltages $V_0 = 0$ V to 5 V.

© 2006 WILEY-VCH Verlag GmbH & Co. KGaA, Weinheim

In Fig. 2 is shown the steady-state current–voltage characteristic as well as the differential resistance of the device. For applied voltages less than 2.3 V, the junction can be considered as non-conducting. In a real device, leakage currents determine the total current value. Their contribution is dominant for small bias voltages. From 2.5 V to 6 V, the increasing of the current is weaker than for an exponential law, with a slope monotonically reducing with the bias.

The evolution of the conduction band edge with applied voltage, Fig. 3, corresponds to the behaviour of the current–voltage characteristic of the simulated device. From 0 V to roughly 2.5 V, most part of the voltage drop takes place in the hole transport layer, which is therefore the most resistive region of the structure for that bias range, while the distribution of the electric field does not much vary. The curves for V_0 = 3 V and 4 V show an increasing effect of the applied voltage on the electron transport layer. In the same time, the electric field is nearly zero in the whole α-NPD layer. For V_0 = 5 V, the hole transport layer follows the bias again. This leads to an increasing of the hole drift current which contributes to the total current. The results shown in Fig. 3 also allows us to deduce the variation, in direction and magnitude, of the electrical field (not shown here) in the region where radiative recombination occurs, i.e. roughly between x = 0 nm and x = 5 nm. Such an evolution with the applied bias has of course an effect on the intensity of the light output.

3.3 Impedance and admittance curves

As typical results, we show in Figs. 4 and 5 the curves representing, respectively, Re Z and the capacitance C as function of the frequency f for voltages V_0 between 0 V and 5 V. In Fig. 4, the curves for V_0 = 0 V and 1 V are quite similar. The low-frequency value of Re Z reduces from 2×10^7 Ω to 10^3 Ω for intermediate frequencies, a regime which ends at frequencies of about 3×10^3 Hz. For V_0 = 3 V and 4 V, the low-frequency value of Re Z reduces to, respectively, 400 Ω and 80 Ω, a value which is maintained up to 10^4–10^5 Hz. The result for 5 V is similar to that of 4 V. The corresponding curve is not shown in Fig. 4 for the sake of clarity. In the high-frequency regime, three distinct shapes can be observed, depending on the applied voltage. The Re Z curves for 0 V and 1 V both follow a rapid decrease while the curves for 2 V and 3 V present a shoulder around 10^6 Hz. The results for 4 V and 5 V show a decrease in the region of the highest frequencies.

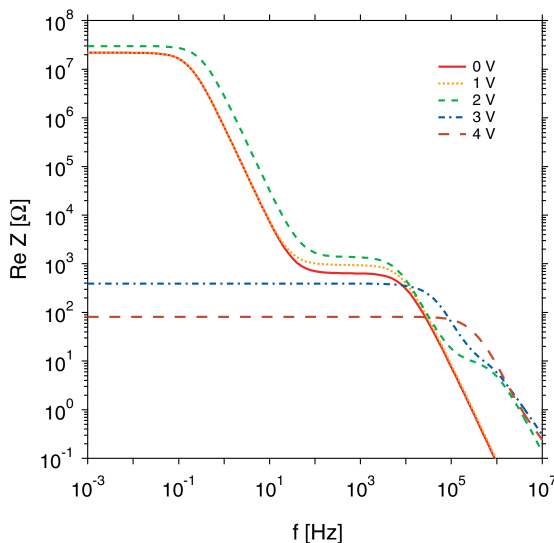

Fig. 4 Real part of impedance Z as function of frequency f for applied steady-state voltages V_0 = 0 V to 4 V.

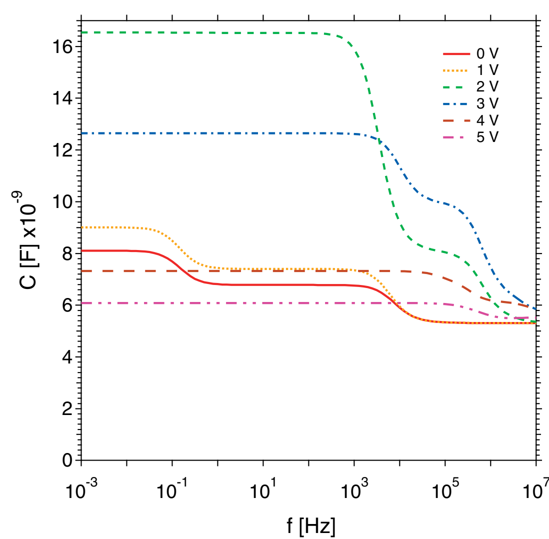

Fig. 5 Capacitance C as function of frequency f for applied steady-state voltages V_0 = 0 V to 5 V.

 © 2006 WILEY-VCH Verlag GmbH & Co. KGaA, Weinheim

The capacitance-versus-frequency curves for the applied voltages $V_0 = 0$ V and 1 V start with low-frequency values of 8.1 nF and 9.0 nF, respectively, and, after two transition frequencies around 10^{-1} Hz and 3×10^3 Hz, reach the high-frequency value of 5.3 nF. The low-frequency values for $V_0 = 3$ V, 4 V and 5 V are, respectively, 12.6 nF, 7.3 nF and 6.1 nF. For these voltages, the decrease to the high-frequency value occurs through a more structured transition. The asymptotic value for very high frequencies is equal to the geometric capacitance $C_{geo} = \varepsilon_r \varepsilon_0 A/d$, obtained with a relative permittivity ε_r equal to 3, a contact area A of 0.2 cm^2 and a total thickness of the organic material of 100 nm. As no free carrier is able to follow the modulation of the external voltage at high frequencies, the material system behaves like a passive dielectric medium. The microscopic origin of the various measurable features is discussed in the next section.

3.4 Charge concentrations and current densities

In Fig. 6, we show as function of position x, the steady-state electron concentration $n_0(x)$ for $V_0 = 0$ V. The hole concentration is too weak at this voltage value to play any role. The real part of the ac amplitude $\tilde{n}$ represents the modification of the local electron concentration which is in phase with the applied ac voltage. The small-signal amplitude $\tilde{V}$ has been chosen real and equal to 10 meV. Re $(\tilde{n})$ is shown for 4 different frequencies, illustrating the different regimes appearing in the capacitance-versus-frequency curve for the same value of the steady-state voltage. At the lowest frequency $f_1 = 1$ mHz, the electron concentration is modulated only in the region from 5 nm to 30 nm, which corresponds to a domain where $n_0(x)$ has not realized its maximum yet. For $f_2 = 1$ Hz, two peaks of equal area but of opposite sign appear on each side of the maximum of $n_0(x)$. At $f_3 = 1.6 \times 10^4$ Hz, the spatial period of the oscillation is approximately twice that for frequency f_2. Finally, for $f_4 = 10^6$ Hz, the amplitude of Re $(\tilde{n})$ has reduced to zero, as the electrons are no longer able to follow the modulation of the applied voltage.

The imaginary part of the complex electron concentration is several orders of magnitude smaller than the real part, at least for $V_0 = 0$ V. The real part of $\tilde{n}(x)$ is generated by the capacitive contribution to the current density. In Fig. 7a, the imaginary part of the current densities are given as function of position x for frequency $f_1 = 1$ mHz. The electron current density is constant from the injecting cathode up to $x = 30$ nm. Then it decreases down to zero over a distance of about 25 nm, which corresponds to the non-

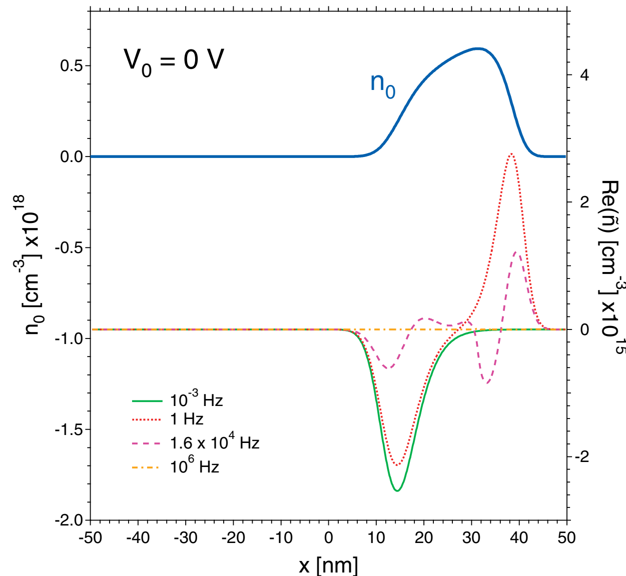

Fig. 6 Steady state electron concentration n_0 and real part of electron concentration amplitude $\tilde{n}$ as function of position x for steady-state applied voltage $V_0 = 0$ V and 4 values of the modulation frequency f.

© 2006 WILEY-VCH Verlag GmbH & Co. KGaA, Weinheim

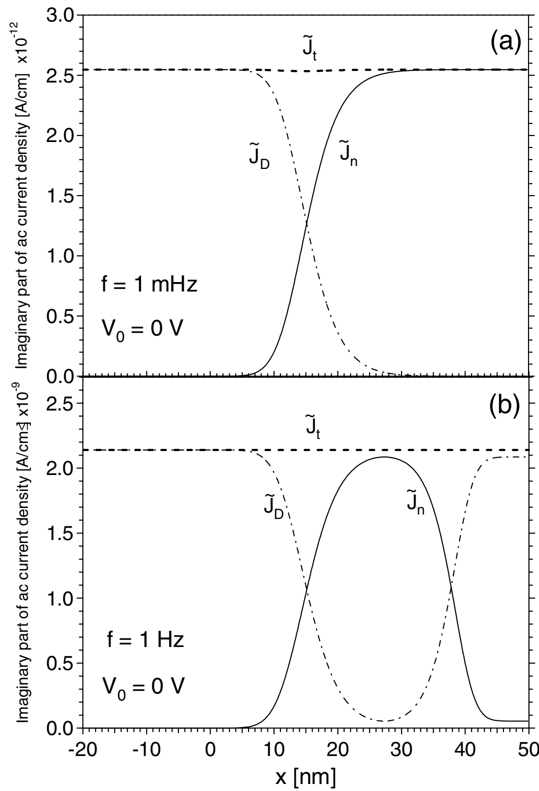

Fig. 7 Imaginary part of the electron current density $\tilde{J}_n$, displacement current density $\tilde{J}_D$ and total current density $\tilde{J}_t$ as function of position x for applied steady-state voltage $V_0 = 0$ V and frequency $f = 1$ mHz (a) and $f = 1$ Hz (b).

zero amplitude of Re ($\tilde{n}$) (Fig. 6). The displacement current density Im (J_D) adds to Im (J_n) to yield the total current Im (J_t) which is constant for all x values. Figure 7b shows the same quantities for $f_2 = 1$ Hz. For this value of the modulation frequency, the amplitude of the imaginary part of the electron current density is non-vanishing only from $x = -5$ to 45 nm. It illustrates the oscillations of the electron concentration between the sides of the steady-state electron density curve $n_0(x)$. Here again, the displacement current density is strong outside this region. No migration of electrons or holes can be observed due to the applied modulating voltage which mainly modifies the electric field in these regions.

The steady-state profiles of the electron and hole concentrations, $n_0(x)$ and $p_0(x)$ are shown for $V_0 = 3$ V in Fig. 8, together with their respective small-signal amplitudes at two different frequencies, i.e. $f_2 = 1$ Hz and $f_5 = 10^5$ Hz. For this value of the bias voltage, the device undergoes strong injection of both charge carriers. This is illustrated by the high general level of the electron and hole concentrations in the structure. The presence of the abrupt interface leads to an accumulation of free charges in the region around $x = 0$ nm: electrons on the x-positive side and holes on the x-negative side. As the hole barrier, resulting from the discontinuity of the valence band edge, is smaller than the electron barrier, holes spread over the interface and recombine with the electrons in the Alq_3 material. For frequency f_2, the amplitude of Re ($\tilde{n}$) reaches its strongest value around 3 nm, very close to the interface. Several other extrema, smaller in magnitude, occur between $x = 10$ and 50 nm. For higher frequency, their positions are shifted, as illustrated by the curve for frequency f_5. In this example, the peak closest to the interface reaches its maximum value for $x = 2$ nm while the other ones are shifted to 25, 32 and 38 nm. The real part of the hole complex amplitude is important in the α-NPD material and leads, for all frequencies, to a strong negative extremum on the x-negative side of the junction.

At this value of the steady-state voltage, the real part of the ac current is stronger than the imaginary part by a factor of 5. Its space-dependence is similar to that of the steady-state components. The imaginary parts of the current densities at all frequencies are in accordance with the real part of the modulated

 © 2006 WILEY-VCH Verlag GmbH & Co. KGaA, Weinheim

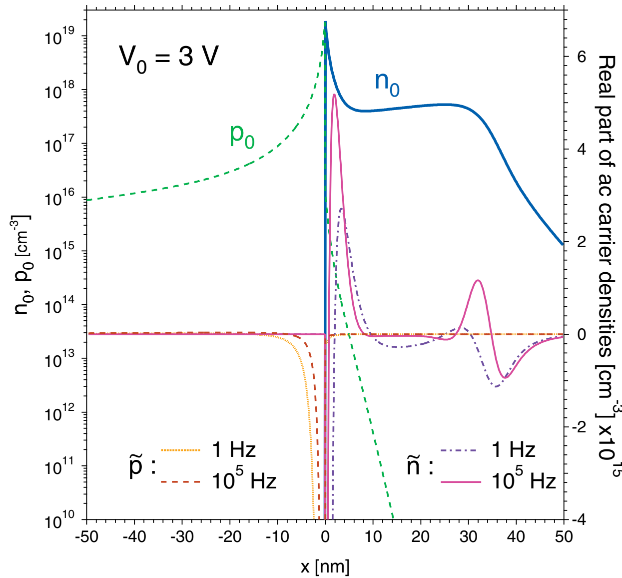

Fig. 8 Steady state electron concentration n_0, hole concentration p_0 for steady-state applied voltage $V_0 = 3$ V and real part of electron amplitude $\tilde{n}$ and hole amplitude $\tilde{p}$ for frequencies of 1 Hz and 10^5 Hz.

electron and hole concentrations. The electron contribution J_n mostly consists of a current between the maximum value of n_0 around 30 nm and the maximum close to the x-positive side of the interface. The applied ac voltage mainly leads to an oscillation of the electron density between these two regions while the hole current allows to fill and empty the accumulation layer located near the interface. The displacement current yields the complementary part which is needed to obtain a total current density constant with for all x values.

3.5 Equivalent circuit modelling

The electrical characteristics can be reproduced by electrical equivalent circuits, composed of resistances and capacitances arranged in parallel or in series. This procedure is frequently applied in the analysis of experimentally obtained admittance or impedance curves. The choice of the equivalent circuit to model the electrical response of a device is not unique in all cases. Different circuits may give acceptable agreement with experiment for a given structure. The association of the various elements of the circuit with a part of the device requires some intuition. In our case, the advantage is that one knows what the devices are built of and it is possible to verify by calculation the interpretation of the model.

In Fig. 9, we show for $V_0 = 0$ V, the calculated real and imaginary parts of the impedance Z, together with the fitted curve. The latter is obtained from a circuit composed of two parallel RC circuits in series, to which a third capacitance C_3 in series is added (inset). The values shown in Fig. 9 are obtained by the fit procedure for the resistances and capacitances with an accuracy as high as 1%. Using these values to calculate the total capacitance C and G/ω, as defined by relation (20), one obtains the fitted values which are shown together with those obtained from the calculation in Fig. 10. This equivalent circuit model is of course only appropriate to describe a device which is non-conducting in the steady state, which means in our case only for V_0 voltages below 2 V. The high-frequency value C_{HF} is the geometrical capacitance C_{geo}, as already mentioned above. The low-frequency value C_{LF} is equal to the value of the isolated capacitance $C_3 = 8.1$ nF. The intermediate value C_{IF} verifies the relation, resulting from elementary circuit analysis

$$C_{\mathrm{IF}} = (1/C_3 + 1/C_1)^{-1} .$$

© 2006 WILEY-VCH Verlag GmbH & Co. KGaA, Weinheim

Editor's Choice

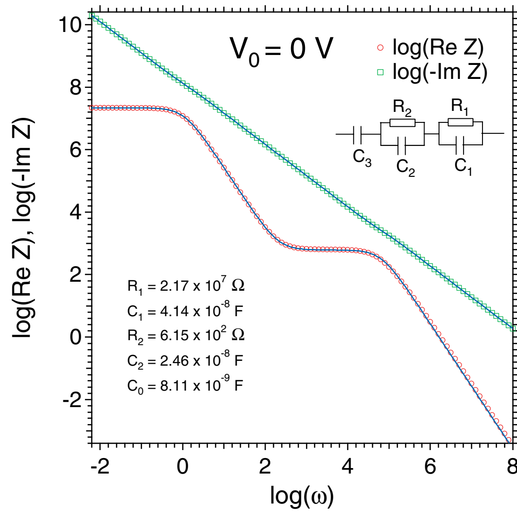

Fig. 9 Calculated real (circles) and imaginary (squares) part of impedance Z as function of angular frequency ω for V_0 = 0 V and fit for equivalent electrical circuit (full lines). Inset shows equivalent circuit used for modelling.

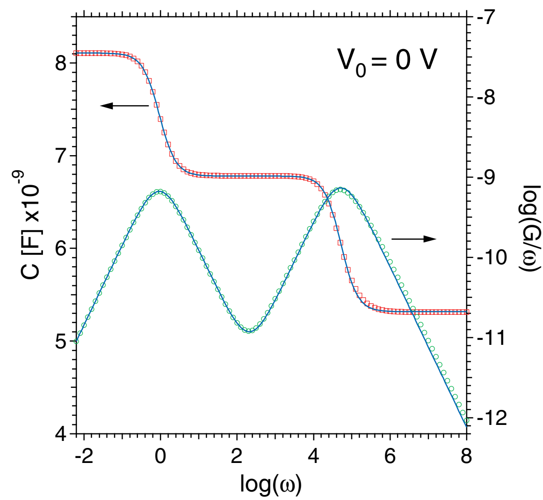

Fig. 10 Calculated capacitance C (squares) and conductance G (circles), divided by angular frequency ω, as function of angular frequency ω for V_0 = 0 V and fit for equivalent circuit (full lines).

The capacitance C_3 corresponds to the depleted region which extends from the anode at x_L to x = 15.5 nm in the Alq_3 layer, as can be seen on the energy band diagram of Fig. 1. Inserting $d = d_3 \equiv 65.5$ nm in the standard capacitance relation $C = \varepsilon_r \varepsilon_0 A/d$ effectively yields the value of C_3. The value of C_1 corresponds to the depletion region at the cathode junction, which extends over a width d_1 = 12.9 nm. R_1 is therefore the associated differential resistance of the contact. The remaining elements R_2 and C_2 correspond to the doped Alq_3 region, with the remaining thickness d_2 = 21.6 nm. The resistance value of R_2 can be checked by numerical integration of the expression

$$R = \frac{1}{Aq} \int_{x_1}^{x_2} \frac{1}{n(x)\,\mu_n(x) + p(x)\,\mu_p(x)}\,\mathrm{d}x, \tag{21}$$

where x_1 and x_2 are the limits of the region under consideration. The fit in this case works well as the device consists of three regions whose properties are strongly different from each other and are delimited by evident boundaries. We can also notice that the R_1C_1 and R_2C_2 circuits reproduce well the regions where Re Z varies with the frequency. Indeed, these transition zones are characterized by the respective cutoff frequencies $f_{c1} = 1/(2\pi\, R_1C_1)$ and $f_{c2} = 1/(2\pi R_2C_2)$. They correspond to peaks in the imaginary part of impedance Z. However, in the results of this structure for zero applied voltage, the frequency response of Im Z is dominated by the contribution of capacitance C_3.

In Figs. 11 and 12, we show the corresponding results for the case V_0 = 3 V. The equivalent circuit now consists of four parallel RC circuits connected in series. The circuit R_1C_1 with the highest resistance value corresponds to the region which includes the depletion zone of the cathode contact as well as the most important part of the electron transport layer and extends over 48.5 nm. The elements R_2 and C_2 represent the remaining part of the Alq_3 layer which is closest to the interface and whose width is of 1.5 nm. The circuit R_3C_3 is associated to the hole transport layer having respective thickness d_3 = 15 nm and R_4C_4 is related to the anode contact, whose depletion region has a width of about 35 nm. In this case the interpretation is less evident as the separations between the different regions are not as abrupt as in the V_0 = 0 V case.

 © 2006 WILEY-VCH Verlag GmbH & Co. KGaA, Weinheim

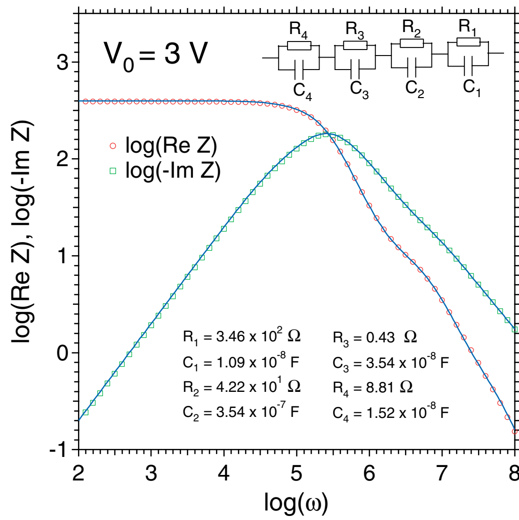

Fig. 11 Calculated real (circles) and imaginary (squares) part of impedance Z as function of angular frequency ω for $V_0 = 3$ V and fit for equivalent electrical circuit (full lines). Inset shows equivalent circuit used for modelling.

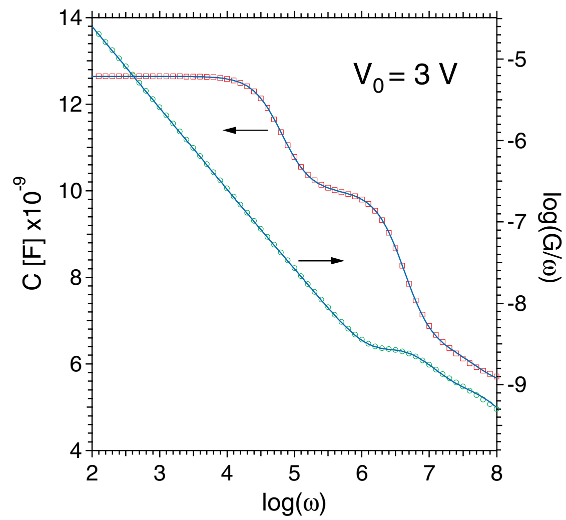

Fig. 12 Calculated capacitance C (squares) and conductance G (circles), divided by angular frequency ω, as function of angular frequency ω for $V_0 = 3$ V and fit for equivalent circuit (full lines).

In Fig. 13, we compare, for steady-state voltage of 3 V, the frequency response of Re Z obtained by modifying one particular parameter in the numerical simulation. The reference curve, corresponding to the values of the parameters given in Table 1, is denoted by (A). Curve (B) results from the situation where the electron mobility in Alq_3 is multiplied by a factor of 10. As a consequence, we observe a reduction of the value of the plateau at low-frequency, which is related to the differential resistance of the system. This goes with the shift of the first cutoff, located around 10^5 Hz in the reference case, to higher frequencies. However, the position of the second cutoff which occurs between 10^6 Hz and 10^7 Hz in curve (A) has not changed, which means that the reduction in the total resistance at low frequency is

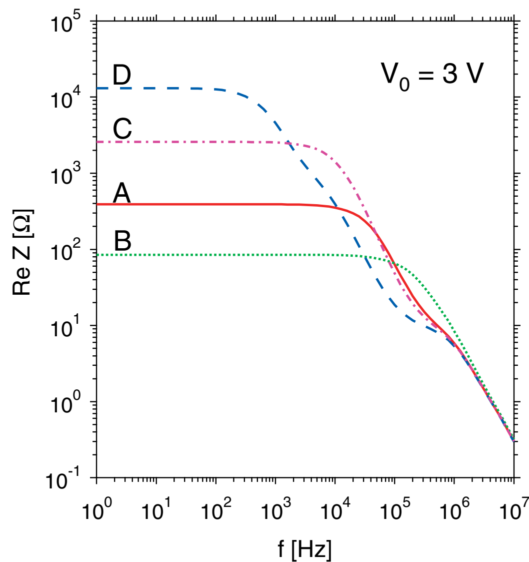

Fig. 13 Re Z as function of frequency f for reference structure (A) calculated with parameters of Table 1, structure with electron mobility of Alq_3 multiplied by factor 10 (B), structure with thickness of Alq_3 layer of 100 nm (C), structure with tunneling coefficient $\alpha_b = 1.5$ (D).

© 2006 WILEY-VCH Verlag GmbH & Co. KGaA, Weinheim

essentially due to the decrease of at least one of the most important resistive components of the electrical circuit. Doubling the thickness of the Alq_3 layer leads to curve (C) where the low-frequency limit has increased by a factor of 6.5. In that region of the spectrum, the signal is dominated by the most important resistance which is the main contribution to the real part of the total impedance, therefore the position of the cutoff shifts only slightly to lower frequencies. Here again, the shape of the high-frequency part of the signal remains relatively unchanged. Curve (D) is obtained by taking the factor α_b in the expression of the tunnel current at the cathode equal to 1.5. This modification leads to a major increase of the resistances at low frequency and a shift of the corresponding cutoff frequencies. The modified Re Z function presents more features than the reference curve. This is due to the greater difference between the values of the resistances which determine the shape of the impedance response in the low-frequency regime, yielding two distinct cutoff transitions in curve (D).

4 Conclusions

We have presented the formal developments which are at the basis of numerical simulation of steady-state and small-signal analysis of organic diodes. Application is made to a two-layer structure whose layers are respectively α-NPD and Alq_3. As results, the microscopic response of the structure and the frequency-dependent impedance and admittance curves are shown. The latter are fitted by equivalent circuit models, leading to the association of particular regions of the device with each of the elements. This analysis may be useful in the interpretation of the experimentally-obtained admittance curves, and may help in the assessment of the quality of a contact or the conductivity of a particular region. In the best situations this could allow to obtain the value of parameters corresponding to the description of contacts or of one of the constituting materials.

The formalism could be applied to more complex systems, composed of more than two layers, including interface layers or deep traps with either discrete or continuous energy distributions [29]. Furthermore, the implementation of additional features, such as generalized Einstein relations [30, 31] or dependence of mobility with charge density [32], would be possible extensions to the present work.

Acknowledgement Financial support by INTERREG III Project EMR INT III 0304-2.1.57 is gratefully acknowledged.

References

[1] W. Brütting, S. Berleb, and A. G. Mückl, Org. Electron. **2**, 1 (2001).
[2] D. M. Taylor and H. L. Gomes, J. Phys. D **28**, 2554 (1995).
[3] I. H. Campbell, D. L. Smith, and J. P. Ferraris, Appl. Phys. Lett. **66**, 3030 (1995).
[4] M. G. Harrison, J. Grüner, and G. C. W. Spencer, Synth. Met. **76**, 71 (1996).
[5] M. Meier, S. Karg, and W. Riess, J. Appl. Phys. **82**, 1961 (1997).
[6] J. Scherbel, P. H. Nguyen, G. Paasch, W. Brütting, and M. Schwoerer, J. Appl. Phys. **83**, 5045 (1998).
[7] C. Jonda and A. B. R. Mayer, Chem. Mater. **11**, 2429 (1999).
[8] S. H. Kim, K. H. Choi, H.-M. Lee, D. H. Hwang, L. M. Do, H. Y. Chu, and T. Zyung, J. Appl. Phys. **87**, 882 (2000).
[9] H. W. Rhee, K. S. Chin, S. Y. Oh, and J.-W. Choi, Thin Solid Films **363**, 236 (2000).
[10] R. Ono, M. Kiy, I. Biaggio, and P. Günter, Mater. Sci. Eng. B **85**, 144 (2001).
[11] J. Drechsel, M. Pfeiffer, X. Zhou, A. Nollau, and K. Leo, Synth. Met. **127**, 201 (2002).
[12] S. H. Kim, J. W. Jang, K. W. Lee, C. E. Lee, and S. W. Kim, Solid State Commun. **128**, 143 (2003).
[13] S. Grecu, M. Bronner, A. Opitz and W. Brütting, Synth. Met. **146**, 359 (2004).
[14] A. el Hakim, I. Thurzo, T. U. Kampen, and D. R. T. Zahn, Appl. Surf. Sci. **234**, 149 (2004).
[15] S. H. Kim, S. C. Lim, J. H. Lee, and T. Zyung, Curr. Appl. Phys. **5**, 35 (2005).
[16] A. B. Walker, A. Kambili, and S. J. Martin, J. Phys.: Condens. Mater. **14**, 9825 (2002).
[17] S. Selberherr, Analysis and Simulation of Semiconductor Devices (Wiley, New York, 1981).
[18] J. Shen and J. Yang, J. Appl. Phys. **83**, 7706 (1998).
[19] E. Tutis, M. N. Bussac, B. Masenelli, M. Carrard, and L. Zuppiroli, J. Appl. Phys. **89**, 430 (2001).

 © 2006 WILEY-VCH Verlag GmbH & Co. KGaA, Weinheim

[20] C. D. J. Blades and A. B. Walker, Synth. Met. **111/112**, 335 (2000).
[21] B. Ruhstaller, T. Beierlein, H. Riel, S. Karg, J. Campbell Scott, and W. Riess, IEEE J. Sel. Top. **9**, 723 (2003).
[22] G. Paasch, A. Nesterov, and S. Scheinert, Synth. Met. **139**, 425 (2003).
[23] N. Tessler, D. J. Pinner, and R. H. Friend, Synth. Met. **111/112**, 269 (2000).
[24] D. J. Pinner, R. H. Friend, and N. Tessler, J. Appl. Phys. **86**, 5116 (1999).
[25] M. Schmeits, N. D. Nguyen, and M. Germain, J. Appl. Phys. **89**, 1890 (2001).
[26] J. C. Scott and G. G. Malliaras, Chem. Phys. Lett. **299**, 115 (1999).
[27] L. S. Hung, C. W. Tang, and M. G. Mason, Appl. Phys. Lett. **70**, 152 (1997).
[28] G. Parthasarathy, C. Shen, A. Kahn, and S. R. Forrest, J. Appl. Phys. **89**, 4986 (2001).
[29] M. Sakhaf and M. Schmeits, J. Appl. Phys. **80**, 6839 (1996).
[30] Y. Roichman and N. Tessler, Appl. Phys. Lett. **80**, 1948 (2002).
[31] M. Schmeits, J. Appl. Phys. **80**, 941 (1996).
[32] Y. Roichman, Y. Preezant, and N. Tessler, phys. stat. sol. (a) **201**, 1246 (2004).

Ngoc Duy Nguyen received his Ph. D. from the University of Liege in 2004 under the supervision of Marcel Schmeits. His thesis was realized within the Solid State Physics Group and was devoted to the electrical characterization of heterostructures made of III-nitride compounds. He is now working as a postdoctoral fellow for a European project on organic light-emitting diodes. His current research interests are in the transport properties of organic semiconductors, where the conduction mechanisms and the role of traps are studied using admittance spectroscopy and numerical simulations.

© 2006 WILEY-VCH Verlag GmbH & Co. KGaA, Weinheim